The need for dynamic inflow models for vertical axis wind turbines

Tavernier, D. De; Ferreira, C.

DOI
10.1088/1742-6596/1356/1/012036

Publication date
2019

Document Version
Final published version

Published in
Journal of Physics: Conference Series

The need for dynamic inflow models for vertical axis wind turbines

IOP Conf. Series: Journal of Physics: Conf. Series **1356** (2019) 012036 doi:10.1088/1742-6596/1356/1/012036

The need for dynamic inflow models for vertical axis wind turbines

D. De Tavernier, C. Ferreira

Delft University of Technology, Wind Energy, Kluyverweg 1, 2629HS Delft, The Netherlands

E-mail: d.a.m.detavernier@tudelft.nl

Abstract. This paper investigates the need for dynamic inflow models for vertical axis wind turbines (VAWTs). The approach is two-fold. First, dynamic inflow is realised by dynamic thrust on an actuator disk in OpenFOAM. The induction phase shift and amplitude showed a significant dependency on the streamwise location. Second, a reference turbine in surging motion is studied using an actuator line OpenFOAM model as reference and an actuator cylinder model (with and without dynamic inflow model). The Larsen and Madsen dynamic inflow model is able to capture the overall behaviour in dynamic inflow conditions, however, it may be improved in the most upwind and downwind location. This study indicates that the modelling of VAWTs in dynamic inflow conditions may be enhanced by improving the dynamic inflow models.

Nomenclature

a	=	Axial induction [−]	D	=	Rotor diameter, $2R$ [m]	$t^\star$	=	Non-dimensional time [−]
A	=	Induction amplitude [−]	k	=	Reduced frequency, $^{\omega D}/_{2V_\infty}$ [−]	V_{rel}	=	Relative velocity $[m/s]$
c	=	Chord length $[m]$	Q_n	=	Normal loading [−]	V_∞	=	Incoming velocity $[m/s]$
C_l	=	Lift coefficient [−]	Q_t	=	Tangential loading [−]	α	=	Angle of attack $[deg]$
C_d	=	Drag coefficient [−]	R	=	Rotor radius $[m]$	θ	=	Azimuthal angle $[deg]$
C_P	=	Power coefficient [−]	s	=	Surge $[m]$	σ	=	Rotor solidity, $^{Nc}/_{2R}$ [−]
C_T	=	Thrust coefficient [−]	t	=	Time $[s]$	Φ	=	Phase difference $[deg]$

1. Introduction

Offshore wind turbine technology has made significant progress since the first offshore wind farm installed in 1991. We advanced from fixed platforms to floating structures through a rapid evolution to be able to overcome deeper water depths. Onshore, horizontal axis wind turbines have reached a mature level and dominate the market. Far offshore, the operational conditions are significantly different, raising the question whether other concepts such as vertical axis wind turbines could be more suitable and allow a reduction in the cost of energy.

The development of floating vertical axis wind turbines is still at an early stage. A fundamental difference between onshore and offshore turbines is the additional complexity introduced by the motions of the floating platform [1]. Turbines are translating and rotating in 3 dimensions, as visualised in Figure 1, causing dynamic inflow conditions at the rotor.

1.1. Background

In some modelling techniques such as computational fluid dynamics or vortex methods, phenomena like the dynamic inflow effect are represented since the wake is physically modelled in space and time. However, for fully coupled methods accounting for the aerodynamics,

hydrodynamics, structural dynamics and controller dynamics, these models are too time-consuming making them unsuitable for iterative processes. Simpler models are often opted for, however, they need additional correction models to cope with unsteady effects such as dynamic inflow.

Limited engineering simulation tools are available to perform fully coupled simulations of VAWTs exposed to floating motion; amongst them HAWC2[2], FloVAWT[3], SIMO-RIFLEX-DMS[4] and SIMO-RIFLEX-AC[5]. In these fully coupled methods, the aerodynamic modelling is established using the 2D double multiple-streamtube model or the actuator cylinder model. These (quasi-) steady models are accompanied with dynamic inflow models. The dynamic inflow models opted for by these researchers are derived for horizontal axis wind turbines. To the knowledge of the authors, there is no dynamic inflow model available particularly derived for vertical axis wind turbines.

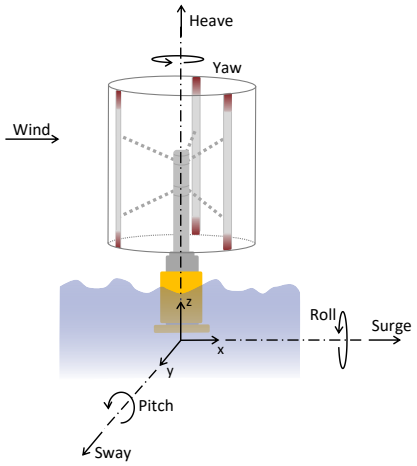

Figure 1: Definition of the platform motions.

1.2. Research objective

It is still unclear whether HAWT dynamic inflow models are applicable to VAWTs, and to what extend they are suitable to deal with the dynamic inflow effect of a VAWT. Therefore, the objective of this paper is:

> *"To identify whether new or improved dynamic inflow models might enhance the modelling of floating vertical axis wind turbines."*

The approach consists of two parts. First, the dynamic inflow effect will be approached theoretically. The flow around a uniformly loaded unsteady actuator disk is studied and the induction at various locations is studied. In the second part of this research, the importance of dynamic inflow models will be quantified using an application. The performance of a VAWT with cyclic motion will be calculated using an OpenFOAM actuator line model and the actuator cylinder with dynamic inflow engineering model, as it is used in the fully coupled simulation tools.

2. Theoretical Approach

2.1. Methodology

Dynamic inflow is often realised by dynamic thrust: a constant incoming wind and an unsteadily loaded actuator. The actuation surface of a VAWT is a cylinder. However, a uniformly loaded actuator cylinder produces exactly the same velocity field as a uniformly loaded actuator disk, since vorticity is only shed at the edges of the actuator disk or at the transition from upwind to downwind for an actuator cylinder. Therefore, it is of non-importance on what surface the forces are applied. The dynamic thrust is realised by applying a time-varying cyclic thrust coefficient on an actuator disk prescribed by a baseline thrust (C_{T0}), amplitude (ΔC_T) and reduced frequency (k). The cases that are considered in this research have a baseline thrust of 1/9 and 7/9, where the first one presents a low loaded case with a small induction and the second one present a highly loaded case with a larger induction. The thrust amplitude is fixed to 1/9. The cyclic loading is applied with four different reduced frequencies, i.e. 0.05, 0.2, 0.5 and 1. The frequency is non-dimensionalised using $k = {}^{\omega D}/_{2V_\infty}$. The expression of the time-varying thrust coefficient is given by Equation 1. In Figure 2, the harmonic loading is visualised as a function of time. The disk diameter is set to 1m and the incoming velocity is 1m/s.

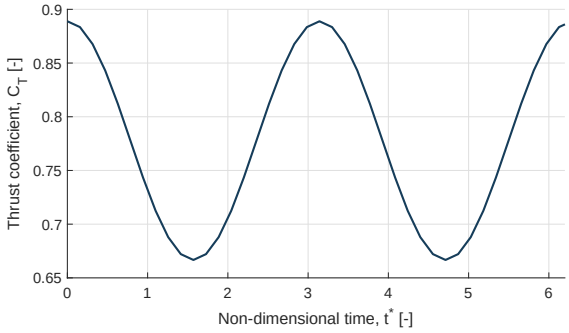

Figure 2: Harmonic time-varying load ($C_{T0} = 7/9$, $\Delta C_T = 1/9$, $k = 1$)

$$C_T(t) = C_{T0} + \Delta C_T \cdot \cos\left(\frac{2\pi k V_\infty}{D} t\right) \quad (1)$$

The flow field is calculated using the computational fluid dynamics (CFD) tool OpenFOAM [6]. A 2D transient solver for incompressible flows is used, namely pisoFOAM. The predefined thrust coefficient is realized by defining uniformly distributed volume forces over the actuator disk region. No turbulence model is applied. The domain has size [-100D, 100D] in width and height. The grid is constructed using blockMesh and is decomposed into a set of one million hexahedral blocks. The grid is dense around the actuator disk and gradually becomes more course away from the disk. The time step is set to $0.0025 V_\infty / R$. This combination of grid and time step has shown to produce converged results. The grid quality is verified by making a comparison with the theoretically expected axial induction at the centre of the disk from the momentum theory for various steady thrust coefficients. The CFD model agrees well with momentum theory for low thrust. The discrepancy is slightly larger for the higher thrust values, with a maximum of 1.5%. For the unsteady cases, the initial conditions are defined using the solution of the steady case with a similar baseline thrust.

A random instant velocity field after some cyclic thrust revolutions is presented in Figure 3. At various locations the axial induction is extracted. In order to quantify the hysterical response, the amplitude and phase delay of the induction with respect to the thrust coefficient are calculated using Lissajous' graphical method[7]. Saying that A is the induction amplitude and C is the zero-crossing height, the phase difference Φ between the induction and thrust is given by Equation 2.

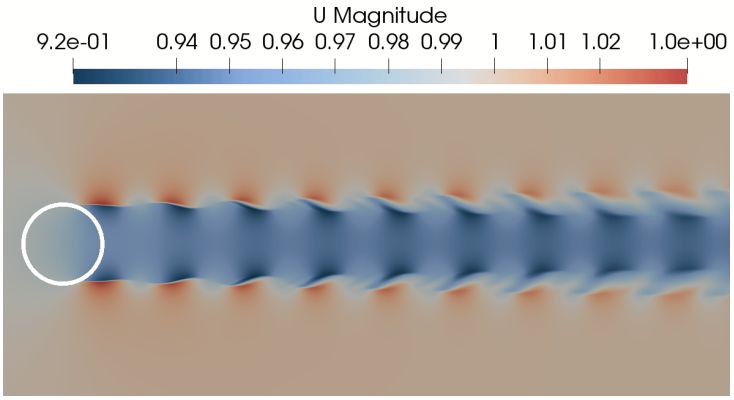

Figure 3: Instant velocity field of a harmonic time-varying load ($C_{T0} = 0.11$, $k = 1$)

$$\Phi = \sin^{-1}\left(\frac{C}{A}\right) \quad (2)$$

The unsteady induction found by the OpenFOAM model will be compared to what is predicted by the dynamic inflow model proposed by Larsen and Madsen[8]. This model is

also used in *SIMO-RIFLEX-AC*[5]. Dynamic inflow is modelled using a low pass filtering of the steady state induced velocities, similar as is done for horizontal-axis wind turbines. The induced velocity filtered for the near and far wake are presented by Equation 3 to Equation 5 in which a_{n-1} denotes the induced velocity of a previous time step. $a_{s,n}$ refers to the steady induced velocity of the current time step and Δt is the size of the time step. τ_{nw} and τ_{fw} are the time constants for the near and far wake filter, respectively and are non-dimensionalised with respect to the rotor radius and average wake velocity ($\tau = {}^{\tau^\star R}/_{V_{wake}}$). The dimensional constants $\tau^\star_{nw}$ and $\tau^\star_{fw}$ are 0.5 and 2. [9]

$$a_{nw} = a_{n-1} \exp\left(-\frac{\Delta t}{\tau_{nw}}\right) + a_{s,n}\left(1 - \exp\left(-\frac{\Delta t}{\tau_{nw}}\right)\right) \tag{3}$$

$$a_{fw} = a_{n-1} \exp\left(-\frac{\Delta t}{\tau_{fw}}\right) + a_{s,n}\left(1 - \exp\left(-\frac{\Delta t}{\tau_{fw}}\right)\right) \tag{4}$$

$$a_n = 0.6a_{nw} + 0.4a_{fw} \tag{5}$$

2.2. Results & Discussion

As a representative example, consider a time-varying load with a baseline thrust C_{T0} of 7/9, a load amplitude ΔC_T of 1/9 and a reduced frequency k of 1. The simulations are run for multiple load cycles until the solution showed a stable and converged amplitude and phase delay between the acquired and previous cycle with an accuracy of 10^{-3}. Only the last cycle is considered for further analysis.

In Figure 4 the axial induction at three different locations are presented: (1) upstream at coordinates (-R,0), (2) at the centre of the disk with coordinates (0,0) and (3) downstream at coordinates (R,0). First of all, it is observed, though not visible in the graphs, that the average induction a_0 downwind is larger than the induction at the centre and upstream. This is however not surprising. In Figure 4(a), the induction is presented as a function of time. From this graph, it is clear that the induction at the three locations is responding significantly different to the cyclic loading. Combining this with Figure 4(b) in which the induction is plotted versus the thrust coefficient, it can be said that the hysteresis loop clearly indicates a different amplitude and phase shift for the different locations. Although that all axial inductions lag the applied thrust coefficient, the induction downwind lags the most, followed by the upwind and consequently the centre location. The normalised induction amplitude is largest at the centre of the disk and rather similar upwind and downwind.

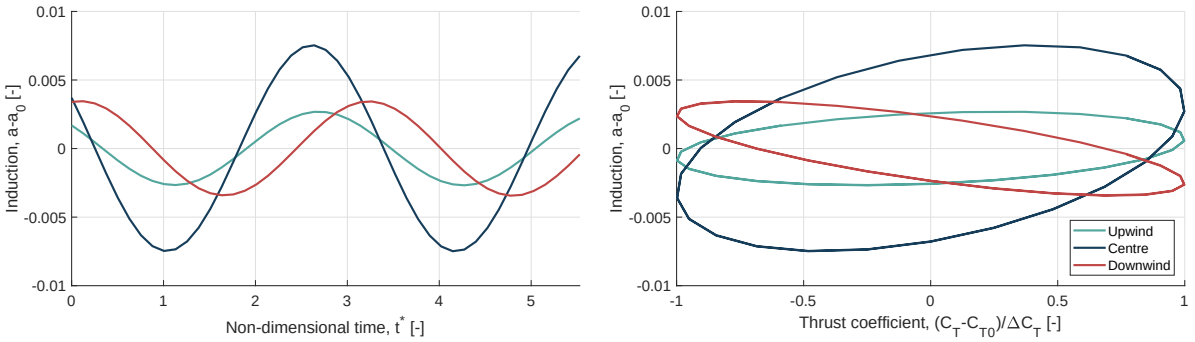

(a) Time vs. induction *(b) Thrust vs. induction*

Figure 4: Resulting induction to harmonic time-varying load at an upwind, centre and downwind location ($C_{T0} = 0.77$, $\Delta C_T = 1/9$, $k = 1$)

Performing similar calculations with different baseline thrust coefficients and reduced frequencies, Figure 5 is made. Figure 5(a) and (b) correspond to a baseline thrust of 1/9 and Figure 5(c) and (d) have a baseline thrust of 7/9. In all figures, the induction of the three locations are plotted. The induction phase shift and amplitude are significantly depending on the reduced frequency. The larger the cyclic frequency of the thrust coefficient is, the larger the phase shift becomes. Also, the induction amplitude decreases with increasing frequency. Similar trends are observed for the two baseline thrust coefficients.

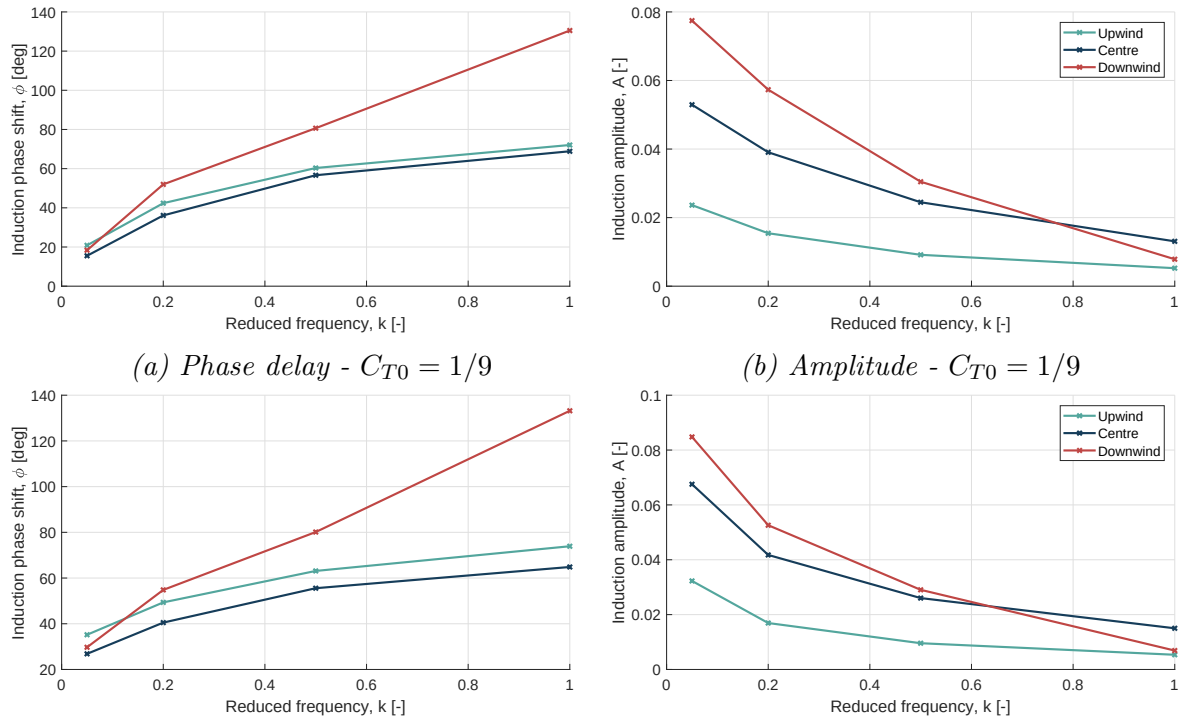

(a) Phase delay - $C_{T0} = 1/9$

(b) Amplitude - $C_{T0} = 1/9$

(c) Phase delay - $C_{T0} = 7/9$

(d) Amplitude - $C_{T0} = 7/9$

Figure 5: Variation of induction phase shift and amplitude to harmonic time-varying load with various reduced frequencies at an upwind, centre and downwind location

So far only 3 locations were considered. In Figure 6, the induction phase shift and amplitude are computed for a range of x-locations. From these figures it can be understood how these parameters are depending on each other. Figure 6(a) and (b) have a baseline thrust coefficient of 1/9 and Figure 6(c) and (d) have a baseline of 7/9. The different lines correspond to different reduced frequencies. One can conclude that away from the rotor centre, the phase shift is increasing. This means that the centre of the rotor is reacting the fastest on a cyclic thrust coefficient compared to its surrounding. Furthermore, the phase shift increases more rapidly downwind than upwind. The increasing rate is rather similar for all frequencies upwind, however, downwind the rate of change of the phase shift increases with increasing frequency. Considering the induction amplitude, one can say that in general the amplitude increases with increasing x-location (from upwind towards downwind). Again, the biggest differences between the different reduced frequencies is downwind. Finally, the two baseline cases show a very similar behaviour.

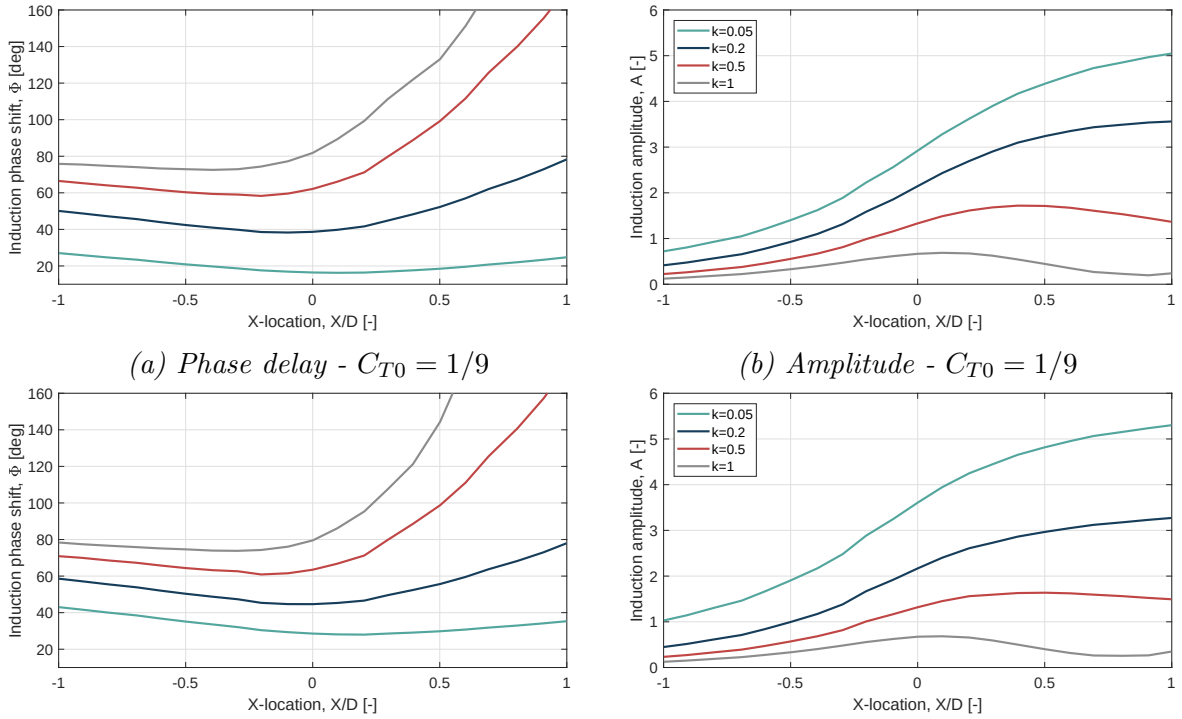

(a) Phase delay - $C_{T0} = 1/9$ *(b) Amplitude - $C_{T0} = 1/9$*

(c) Phase delay - $C_{T0} = 7/9$ *(d) Amplitude - $C_{T0} = 7/9$*

Figure 6: Variation of induction phase shift and amplitude to harmonic time-varying load for various x-locations between -1D and 1D.

Comparing the inductions at the three locations extracted from the unsteady simulations with the induction calculated using the Larsen and Madsen[8] dynamic inflow model (DIM) and the steady induction, Figure 7 is generated. The three figures correspond to three different locations: one upwind, one at the centre and one downwind. The predictions of the dynamic inflow model at the centre match well, however, at the upwind and downwind location, the discrepancies are large. Similar observations are made for the other reduced frequencies and baseline thrust.

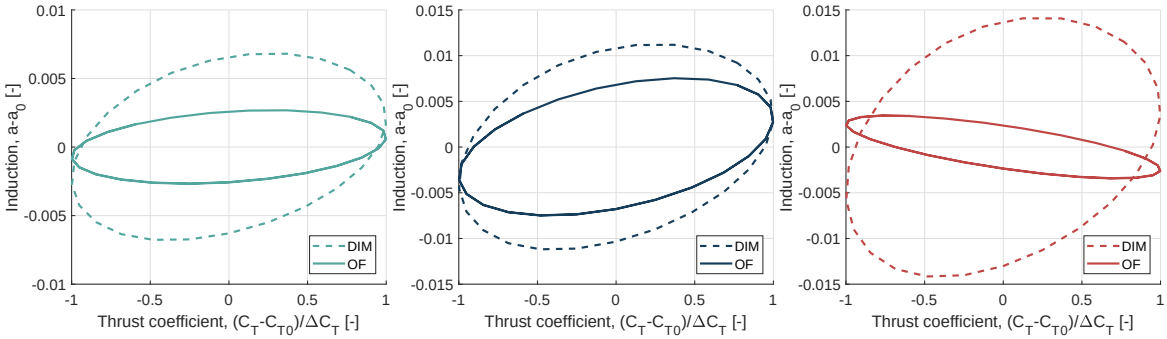

(a) Upwind *(b) Centre* *(c) Downwind*

Figure 7: Comparison of the unsteady induction at the upwind, centre and downwind location from the unsteady OpenFOAM calculations with the steady OpenFOAM calculations corrected using the dynamic inflow model. ($C_{T0} = 0.77$, $\Delta C_T = 1/9$, $k = 1$)

HAWT's dynamic inflow models are derived and tuned to predict the behaviour of dynamic inflow at the rotor disk. This theoretical approach confirms that the behaviour of the induction

upwind and downwind are reacting significantly different then at the centre and this is not captured by the dynamic inflow model. The phase shift difference between the downwind and centre of the rotor goes above 65 degrees while the amplitude might be almost 4 times as large.

3. Practical Approach

3.1. Methodology

The actuator disk approach showed that the dynamic inflow effect on the induction is significantly different at various locations of the rotor and that the dynamic inflow model could not capture the behaviour well at the upwind and downwind position. In this part an application-oriented approach will be taken to quantify what this means for the prediction of the VAWT performance. The performance of a cyclic surging VAWT will be computed using an actuator line model in OpenFOAM as reference and the actuator cylinder model including a dynamic inflow engineering model. The idea behind both codes is similar:(1) determine the force field when the flow field is known and (2) to determine the flow field when the force field is known.

The actuator line model uses the open-source *TurbineFoam* library[10] in OpenFOAM[6]. This model is based on the classical blade element theory and uses a Navier-Stokes description to solve the flow field in time. The blades are represented as lines for which the 2D profile lift, drag and pitching moment are input. The loads are introduced as distributed body forces to the flow field to avoid instability. An extra source term is added to the momentum equation and solved with the pisoFOAM solver. The *TurbineFoam* library includes modules to account for unsteady effects such as dynamic stall, added mass, flow curvature and end effects[11]. Although the model can include struts and a tower, these are excluded for simplicity. For this work, the model is extended to allow turbine motion. The grid is set to [-8D,8D] in freestream direction, [-5D,5D] in radial direction and [-5D,5D] in spanwise direction and contains 17.5 cells per diameter length. Around the rotor and in the turbulent zone, a first order refinement of the mesh is applied. The simulations are run for at least 30 revolutions with a time step every 1 deg azimuthal change. A convergence study on the grid and simulation time step showed that the simulations produced converged results on the power coefficient (variation was below 1E-3).

The Actuator Cylinder model [12], as often used in fully coupled engineering simulation tools, is a 2D flow model extending the actuator disk concept[13]. An actuation surface is introduced that coincides with the swept area of the VAWT rotor. The reaction of the blade forces, derived from simple steady blade element theory, are applied on the flow as distributed body forces. The solution of the induced velocity field builds on the 2D, steady, incompressible Euler equations and the equation of continuity. The induced velocities are prescribed by a linear and non-linear solution for which the *Mod-Lin* solution[12] uses only the linear solution and a correction to account for the non-linear part. As Madsen[12] and later Cheng et al.[14] proposed, also the tangential loading is included into the linear solution of the induced velocities. The steady state induced velocities calculated by the AC model are furthermore compensated for dynamic effects using a Larsen and Madsen dynamic inflow model, as explained earlier.

All simulations are performed on a reference turbine with solidity of 0.1 and tip speed ratio of 3. Dynamic stall and end effects are disregarded for simplicity. The lift and drag are prescribed by $C_l = 1.11 \cdot 2\pi sin(\alpha)$ and $C_d = 0$. The comparison of the 2D actuator cylinder model is performed with respect to the mid-section of the 3D actuator line OpenFOAM model to approach 2D conditions the most. For this reference turbine, the predictions of both codes for non-surging conditions (excluding dynamic inflow) are very similar. Figure 9 presents a comparison. The power and thrust coefficient calculated by the actuator cylinder model are 0.54 and 0.73, respectively. For the actuator line OpenFOAM model this is 0.52 and 0.72, respectively. The reference turbine is subjected to a cyclic surging mode given by Equation 6 and visualised by Figure 8. This expression is similar as the cyclic thrust equation used before.

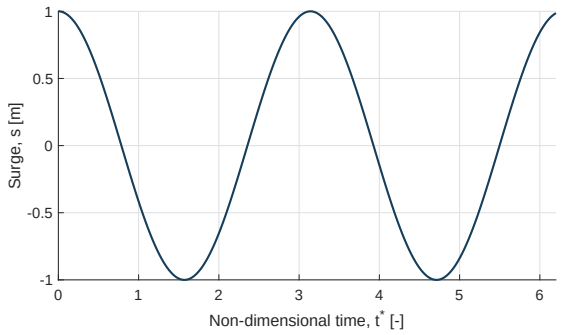

$$s = s_0 + \Delta s \cdot \cos\left(\frac{2kV_\infty}{D}t\right) \tag{6}$$

Figure 8: Harmonic time-varying surge motion ($s_0 = 0$, $\Delta s = 1$, $k = 1$)

To assess the time response of the actuator cylinder model compared to the actuator line OpenFOAM model, the time response assurance criteria (TRAC) is used, as given by Equation 7[15]. This criteria is used for assessing the similarity of two time signals. Values close to 1 indicate high similarity while values close to 0 indicate low similarity. For the reference turbine without surge motion, the TRAC value of the normal and tangential loading time response are both 0.996.

$$TRAC = \frac{\left([t_{AC}]^T[t_{OF}]\right)^2}{\left([t_{AC}]^T[t_{AC}]\right)\left([t_{OF}]^T[t_{OF}]\right)} \tag{7}$$

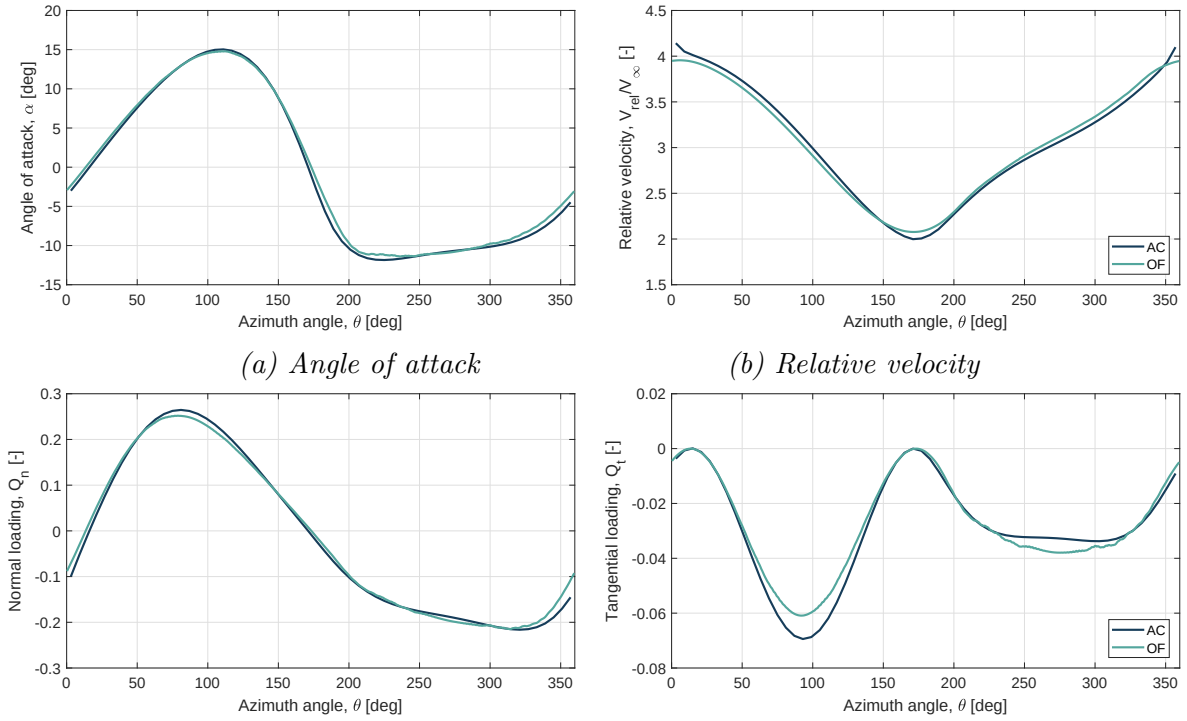

(a) Angle of attack *(b) Relative velocity*

(c) Normal loading *(d) Tangential loading*

Figure 9: Comparison between actuator cylinder (AC) and actuator line OpenFOAM (OF) model for a VAWT with a solidity of 0.1, tip speed ratio of 3.0. $C_l = 1.11 \cdot 2\pi sin(\alpha), C_d = 0$

3.2. Results & Discussion

To quantify the capabilities to compute the performance of a VAWT in dynamic inflow conditions with an engineering model derived for HAWTs, the reference turbine is subjected to a surging motion with various reduced frequencies. The resulting loads are presented in Figure 10(a) and (b) for a reduced frequency of 1.0 and in Figure 10(c) and (d) for a reduced frequency of 2.0. The results of three models are presented: (1) the actuator line OpenFOAM model as reference, (2) the actuator cylinder model without dynamic inflow model and (3) the actuator cylinder model with dynamic inflow model. As expected, the effect of the dynamic inflow model is larger for an increasing reduced frequency. This is clearly recognised by comparing the results with and without the dynamic inflow model. It may be argued that the simple dynamic inflow model implemented here, is capable of capturing the overall trends of the dynamic effects. The current model seems to be able to predict the behaviour at the rotor edges well, however, at the most upstream and downstream position, the model still lags accuracy and can be improved further. At some time steps, the actuator cylinder model without dynamic inflow model outperforms the one including the dynamic inflow model causing the prediction of the average tangential loading, which is a measure for the average power coefficient, not to be improved significantly.

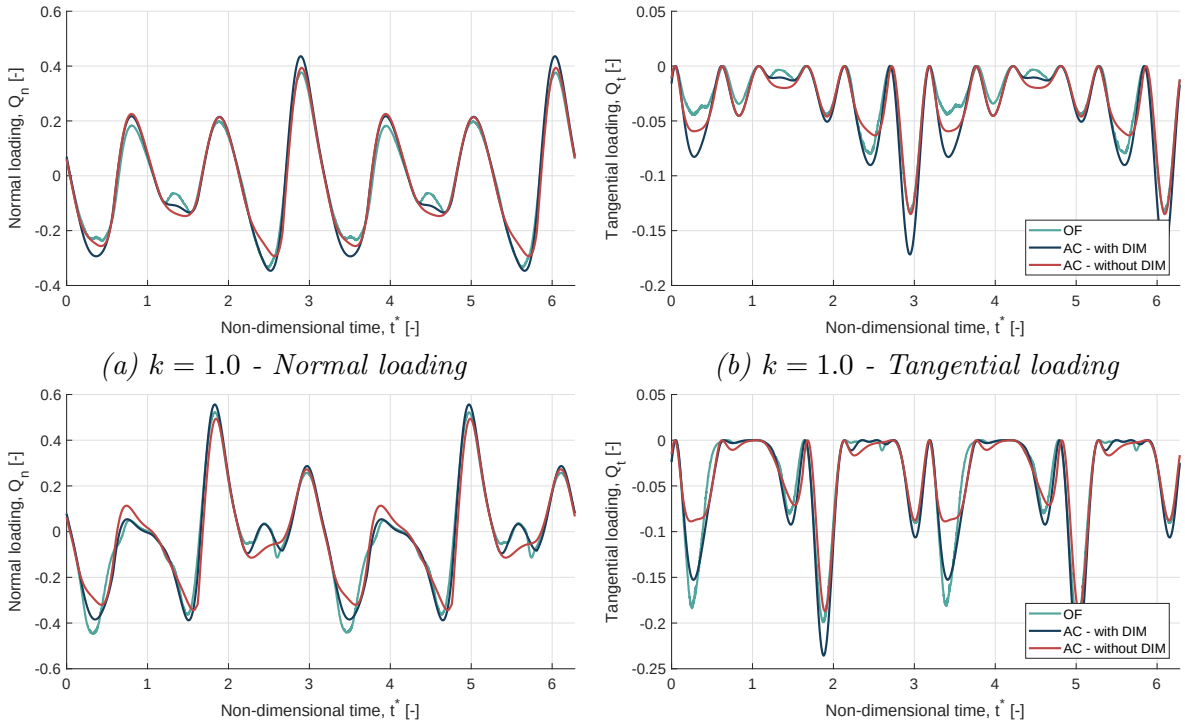

(a) $k = 1.0$ *- Normal loading*

(b) $k = 1.0$ *- Tangential loading*

(c) $k = 2.0$ *- Normal loading*

(d) $k = 2.0$ *- Tangential loading*

Figure 10: Comparison between actuator cylinder with dynamic inflow model (AC-with DIM), without dynamic inflow model (AC-no DIM) and actuator line OpenFOAM (OF) model for a VAWT with a solidity of 0.1, tip speed ratio of 3.0. Surging motion with $s_0 = 0$, $\Delta s = 1$. $C_l = 1.11 \cdot 2\pi sin(\alpha), C_d = 0$.

To quantify this further, the time response assurance criteria is considered. Without surging motion the TRAC value of the normal and tangential loading response is 0.996, saying there is a strong similarity between the predictions of the actuator cylinder model and the actuator line OpenFOAM model. When increasing the reduced frequency of the surging motion, this TRAC value decreases, up to 10% for a reduced frequency of 2. The model with dynamic inflow model clearly outperforms the one without engineering model. The overall prediction is improved

according to the TRAC value, however, it is still lower than the non-surging case, especially at the larger reduced frequencies. This indicates that there is still room for improvement on the dynamic inflow model and as such a new engineering model might reach a better accuracy level with the actuator cylinder model in dynamic inflow conditions.

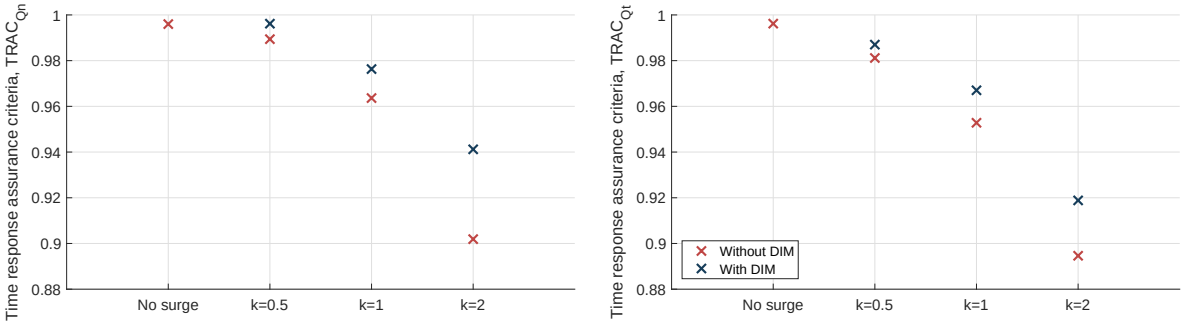

(a) TRAC normal loading *(b) TRAC tangential loading*

Figure 11: Time response assurance criteria between actuator line OpenFOAM (OF) and actuator cylinder (AC) model with and without dynamic inflow model for various reduced frequency on the normal and tangential loading time series

4. Conclusion

Fully coupled simulation tools for VAWTs often employ engineering models to account for the dynamic inflow effect. This paper investigates to what extend dynamic inflow models derived for HAWTs capture the dynamic effects of VAWTs and whether new dynamic models may be beneficial to enhance the modelling of VAWTs in dynamic inflow conditions.

From a theoretical approach, in which the velocity field around an unsteady uniformly loaded actuator disk is studied using 2D CFD calculations, it is found that the induction at an upwind location, at the disk centre and downwind the disk are behaving differently. The induction amplitude and phase shift with respect to the applied thrust are not only depending on the baseline thrust and reduced frequency, but also on the location of interest. Since HAWT dynamic inflow models are derived and tuned with respect to the centre of the rotor disk, the Larsen and Madsen HAWT dynamic inflow models was able to capture the behaviour at the centre well but not upwind and downwind.

To quantify the effect of using a time filtering dynamic inflow model, the performance of a cyclic surging VAWT is computed using an actuator line model in OpenFOAM as reference and the actuator cylinder model including a dynamic inflow engineering model. The TRAC value of the normal and tangential loading revealed that current dynamic inflow models already capture the overall behaviour better. However, at some time steps, the actuator cylinder model without dynamic inflow model still outperforms the one including the dynamic inflow model causing the prediction of the average tangential loading, which is a measure for the average power coefficient, not to be improved.

With this, it is identified that there might be a value in improving the existing engineering models and develop a dynamic inflow model specifically designed for vertical-axis wind turbines. This might allow to enhance the modelling of floating vertical axis wind turbines where dynamic inflow plays an important role.

References

[1] J. Cruz, M. Atcheson, Floating Offshore Wind Energy: The next generation of wind energy, Springer, 2016.

[2] H.A. Madsen, T.J. Larsen, U.S. Paulsen, L. Vita, Implementation of the actuator cylinder flow model in the HAWC2 code for aero-elastic simulations on vertical axis wind turbines. In 51st AIAA Aerospace Sciences Meeting including the New Horizons Forum and Aerospace Exposition, 2013.
[3] M. Collu, M. Borg, A. Shires, F.N. Rizzo, E. Lupi, FloVAWT: further progresses on the development of a coupled model of dnamics fro floating offshore VAWTs, Proceedings of the ASME, June 2014.
[4] K. Wang, Modelling and dynamic analysis of a semi-submersible floating vertical axis wind turbine, PhD thesis, Norwegian University of Science and Technology, January 2015.
[5] Z. Cheng, Integrated dynamic analysis of floating vertical axis wind turbines, PhD thesis, Norwegian University of Science and Technology, March 2016.
[6] The OpenFOAM Foundation Ltd, OpenFOAM v6, 2018, `https://openfoam.org`.
[7] H. Al-Khazali, M. Askari, Geometrical and graphical representations analysis of Lissajous figures in rotor dynamic system, IOSR Journal of Engineering, Vol.2(5) p971-978, May 2012.
[8] T.J. Larsen, H.A. Madsen, On the way to reliable aeroelastic load simulation on VAWTs, Proceedings of EWEA, 2013.
[9] Z. Cheng, H.A. Madsen, Z. Gao, T. Moan, A fully coupled method for numerical modeling and dynamic analysis of floating vertical axis wind turbines, Renewable Energy, Vol.107 p604-619, 2017.
[10] P. Bachant, A. Goude, M. Wosnik, turbinesFoam/turbinesFoam Version v0.0.8, Zenodo, `http://doi.org/10.5281/zenodo.1210366`, March 2018.
[11] P. Bachant, A. Goude, M. Wosnik, Actuator line modeling of vertical-axis turbines, arXiv preprint 1605.01449, May 2016.
[12] H.A. Madsen, On the ideal and real energy conversion in a straight bladed vertical axis wind turbine, Phd thesis, Aalborg University, 1983.
[13] R. Froude, On the part played in propulsion by differences of fluid pressure. Transactions of the Institute of Naval Architects, Vol.30 p390, 1889.
[14] Z. Cheng, H.A. Madsen, Z. Gao, T. Moan, Aerodynamic Modeling of Floating Vertical Axis Wind Turbines Using the Actuator Cylinder Flow Method. Energy Procedia, Vol.94 p531-543, 2016.
[15] C. Chipman, P. Avitabile, Expansion of transient operating data, Proceedings of the IMAC-XXVII, February 2009.